Nanoscale

Accepted Manuscript

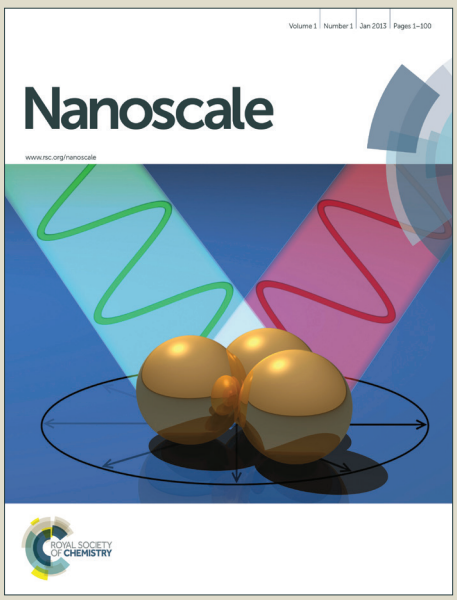

ROYAL SOCIETY OF CHEMISTRY

www.rsc.org/nanoscale

NANOSCALE

RSCPublishing

ARTICLE

Polarized Photocurrent Response in Black Phosphorus Field-Effect Transistors

Cite this: DOI: 10.1039/x0xx00000x

Tu Hong[a], Bhim Chamlagain[b], Wenzhi Lin[c], Hsun-Jen Chuang[b], Minghu Pan[c,*], Zhixian Zhou[b,*], and Ya-Qiong Xu[a,d,*]

Received 00th January 2012,
Accepted 00th January 2012

DOI: 10.1039/x0xx00000x

www.rsc.org/

We investigate electrical transport and optoelectronic properties of field effect transistors (FETs) made from few-layer black phosphorus (BP) crystals down to a few nanometers. In particular, we explore the anisotropic nature and photocurrent generation mechanisms in BP FETs through spatial-, polarization-, gate-, and bias-dependent photocurrent measurements. Our results reveal that the photocurrent signals at BP-electrode junctions are mainly attributed to the photovoltaic effect in the off-state and photothermoelectric effect in the on-state, and their anisotropic feature primarily results from the directional-dependent absorption of BP crystals.

Two dimensional (2D) layered crystals have become one of the most attractive materials for future electronics and optoelectronics due to their unique properties. Graphene, a 2D carbon crystal, has shown extremely high charge-carrier mobility, optical transparency, and broadband absorption.[1-5] However, a zero band gap and ultrafast recombination of the photoexcited electron–hole pairs limit graphene's potential in field effect transistor (FET) applications and photovoltaic generation.[6, 7] FETs made from 2D transition metal dichalcogenides (TMDCs) show very high on/off current ratios, but their relatively low carrier mobility and sizeable band gap (>1 eV) limit their applications in both electronics and optoelectronics.[8-13] Recently, a new class of 2D layered material, few-layer black phosphorus (BP) or phosphorene, has shown excellent transistor performances.[14-18] Their drain current modulation is comparable to TMDC FETs and the carrier mobility of BP is significantly higher than that of TMDCs.[15] While the band gap of bulk BP is 0.3 eV, its few-layer structures have a thickness-dependent direct band gap ranging from 0.3 eV to 2 eV,[19-22] opening up new opportunities for optoelectronic applications. More interestingly, the electrical and optical conductivities of BP are anisotropic,[14-15,17,20] which is different from other 2D materials that have isotropic in-plane properties.

In this study, scanning tunneling microscopy (STM) measurements are performed on freshly cleaved surfaces of BP crystals to characterize their qualities. We also report electrical transport and scanning photocurrent measurements of FETs made from few-layer BP crystals down to a few nanometers. By exploring the generation mechanisms of anisotropic photocurrent response in BP FETs through spatial-, polarization-, gate-, and bias-dependent photocurrent measurements, we show that BP photocurrent response near the BP-electrode contact area is mainly attributed to the photovoltaic effect (PVE) in the off-state and photothermoelectric effect (PTE) in the on-state, and its anisotropic feature primarily results from the directional-dependent absorption of BP crystals. Our studies indicate that BP will be a promising candidate for thin film electronic, optoelectronic, and thermoelectric devices with unique anisotropic nature.

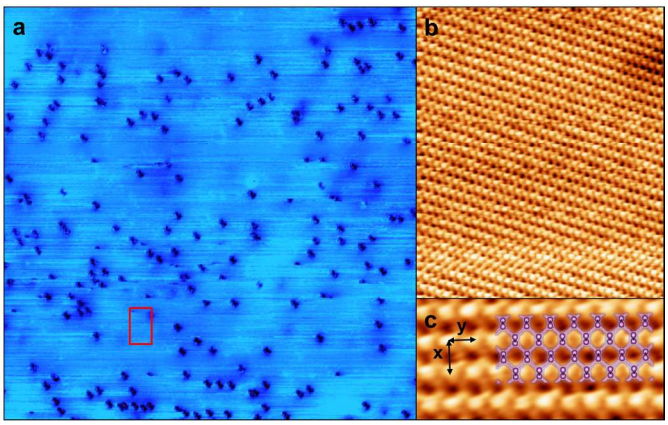

Figure 1. STM images of BP crystals. (a) STM topographic image of a freshly cleaved BP surface with scan size of 240 nm x 240 nm; (b) a zoom-in image of BP with atomic resolution into the flat area marked by red rectangle in (a); and (c) a close-up image showing detailed features of the BP surface structure along x and y directions.

Figure 1a shows a representative STM topographic image of a BP surface, freshly cleaved inside an ultra-high vacuum chamber at room temperature in order to avoid degradation and

placed in a microscope stage overnight at 80 K, where distinct defects are clearly visible in addition to an atomic-flat cleaved plane. Such defects that appear at the fresh-cleaved surface, can only be explained as impurities within BP crystals. Since defects and/or impurities reduce the mean free path of charge carriers and thus mobility by serving as scattering centers for charge transport, extremely low impurity level and high crystalline quality is required for achieving the ultimate device performance.

By zooming into a flat area (marked as red rectangle in Fig. 1a), Figure 1b shows an atomic resolution topographic STM image of BP crystals. As described in the puckered-layer model, an upper phosphorus atom sits just directly above a lower one. Since STM is a surface-sensitive technique, we can assign easily the bright spots in this atomically-resolved image to the upper phosphorus atoms. Therefore, only zigzag atomic chains composed of the upper atoms are visible in the STM image of BP surface. A close-up image (Fig. 1c) reveals more highly resolved features of the surface structure. No surface reconstruction is observed, and all surface phosphorus atoms almost reside in their original sites, as shown in the atomic model.[22] The in-plane lattice constants "x" (along the direction of a lighter effective mass) and "y" (along the direction of a heavier effective mass) measured from the STM image are 4.4 Å and 3.4 Å, respectively, in good agreement with the reported values of bulk BP.[19, 21, 22] Our STM observation agrees very well with the previous STM work.[23]

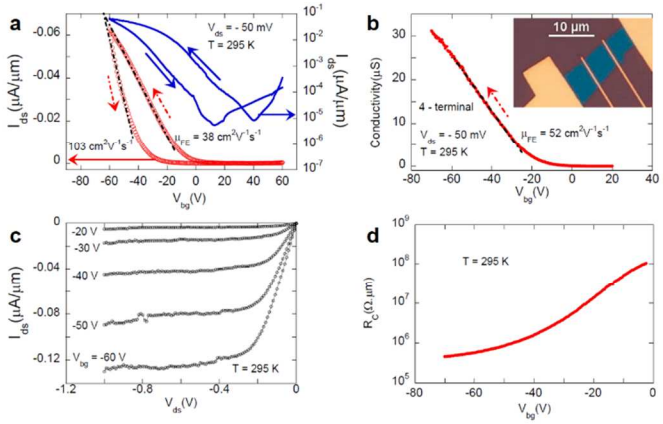

Figure 2. Electrical transport characterization of an 8 nm thick BP FET device at room temperature. (a) Transfer characteristic of the device measured at V_{ds} = -50 mV. (b) Four-terminal conductivity of the device measured with the back-gate voltage sweeping from 20 V to -70 V. Inset: optical micrograph of the device. (c) Output characteristics of the device measured at various gate voltages between -20 and -60 V. (d) Normalized contact resistance of the drain or source contact extracted from the four-terminal measurement.

Ultrathin BP crystals (5 nm - 15 nm thick) were produced by repeated splitting of the above bulk crystals using a mechanical cleavage method, and subsequently transferred to degenerately doped silicon substrates covered with 290 nm SiO_2.[3, 24, 25] Optical microscopy was used to identify thin BP crystals, which were further characterized by Park-Systems XE-70 non-contact atomic force microscopy (AFM). BP FET devices were subsequently fabricated using standard electron beam lithography and electron beam deposition of 5 nm of Ti and 50 nm of Au, where the Si substrate is used as a back gate.[26] To eliminate electrical contact contributions, we also patterned voltage probes in between drain and source electrodes to facilitate four-terminal measurements. An optical micrograph of a typical BP device is shown in the inset of Figure 2b. We chose 5 nm - 15 nm thick BP crystals because multilayer BP of this thickness range has a much higher yield of sufficiently large flakes (for patterning multiple electrodes) and less susceptible to surface oxidation in ambient conditions compared to thinner samples, while still maintaining a reasonably large on/off ratio for FET operations**.** Electrical properties of the devices were measured by a Keithley 4200 semiconductor parameter analyzer in a lakeshore Cryogenic probe station under high vacuum (1×10^{-6} Torr).

Figure 2a shows the electrical transfer characteristics of an 8 nm thick BP FET (as determined by AFM) at room temperature in both linear and semi-logarithmic scales. The device exhibits a predominately *p*-type behavior, with the on/off current ratio achieving 10^4 at a drain-source voltage of -50 mV. The large hysteresis in the transfer characteristics is likely due to charge transfer from neighboring adsorbates (such as moisture and oxygen) or charge injection into the trap sites on the SiO_2 substrate and/or the surface oxidation layer of BP.[16, 27, 28] When the back gate voltage is swept toward the negative direction, a portion of the gate-induced holes are transferred to adsorbates, the surface oxidation layer and/or the substrate to fill the trap sites, leading to a slower rate change of the hole density in the channel (thus a reduced transconductance dI_{ds}/dV_{bg}). The scenario reverses when the gate voltage is swept toward the positive direction. As a result, the field-effect mobility estimated using the expression $\mu = L/W\times dI_{ds}/dV_{bg}/(C_{bg}V_{ds})$ strongly depends on the gate sweep direction, with the mobility extracted from the positive gate sweep direction (103 $cm^2V^{-1}s^{-1}$) being nearly 3 times larger than that extracted from the negative gate sweep direction (38 $cm^2V^{-1}s^{-1}$). Here L= 17.3 μm is the channel length, W = 5.9 μm is the average channel width, dI_{ds}/dV_{bg} is the slope of the I_{ds}-V_{bg} curve in the linear region, and $C_{bg} \approx 1.2\times10^{-8}$ F/cm^{-2} is the capacitance of the Si back gate. To investigate the channel-limited mobility, we also measured the back gate dependence of the conductivity in a four-terminal configuration to eliminate the contact resistance. As shown in Figure 2b, our four-terminal conductivity measurement suggests a mobility improvement from 38 $cm^2V^{-1}s^{-1}$ to 52 $cm^2V^{-1}s^{-1}$ for the negative gate sweep direction. In addition to the defects and/or impurities in the BP crystals, as shown in Figure 1a, other factors such as the surface oxidation and non-ideal BP/dielectric interface may also degrade the mobility. It is worth noting that our transport measurement is performed almost along the y-direction (heavier effective mass), as determined by the polarization-dependent photocurrent measurements below. As reported in previous literatures, the electrical conductivity of BP crystals is highly anisotropic: the mobility along the x-direction (lighter effective mass) is 1.5-1.8 times higher than that along the y-direction (heavier effective mass).[14, 15] Although the field-effect mobility observed in this device is significantly lower than the mobility values for bulk phosphorus crystals, it is comparable to those reported for few nanometer thick BP crystals along the y-direction.[14, 16, 22]

Figure 2c shows the output characteristics of the 8 nm thick device, where the drain-source current is linear at low drain-source voltages and starts to saturate as V_{ds} increases, in qualitatively agreement with the previously reported current saturation behavior in BP FETs.[15] The current saturation is likely caused by the reduction of the effective V_{bg} and V_{ds} due

to the relatively large parasitic series drain/source contact resistance (R_C) given by $V_{bg\_eff} = V_{bg} - R_C I_{ds}$ and $V_{ds\_eff} = V_{ds} - 2R_C I_{ds}$.[29] As shown in Figure 2d, the contact resistance estimated as $R_c = (V_{ds}/I_{ds} - R_{ch})/2$ increases from ≈0.5 MΩ·μm at V_{bg} = -60 V to over 80 MΩ·μm at V_{bg} = -5 V, where V_{ds}/I_{ds} is the total resistance of the device and R_{ch} is the channel resistance extracted from the four-terminal measurement. Such a large contact resistance is expected to considerably reduce V_{bg_eff} and V_{ds_eff}, especially at low V_{bg} and high V_{ds} (e.g. V_{bg} = -20 V and V_{ds} = -1 V), where the voltage drop at the contacts ($R_C I_{ds}$ for V_{bg} and $2R_C I_{ds}$ for V_{ds}) is most significant. At high V_{bg} and low V_{ds}, $R_C I_{ds}$ is relatively small compared to the applied V_{bg} and V_{ds}, leading to nearly linear I_{ds}-V_{ds} characteristics.[30] In addition to the presence of a Schottky barrier, possible sample degradation at the metal contacts may also contribute to the large contact resistance.[14, 16]

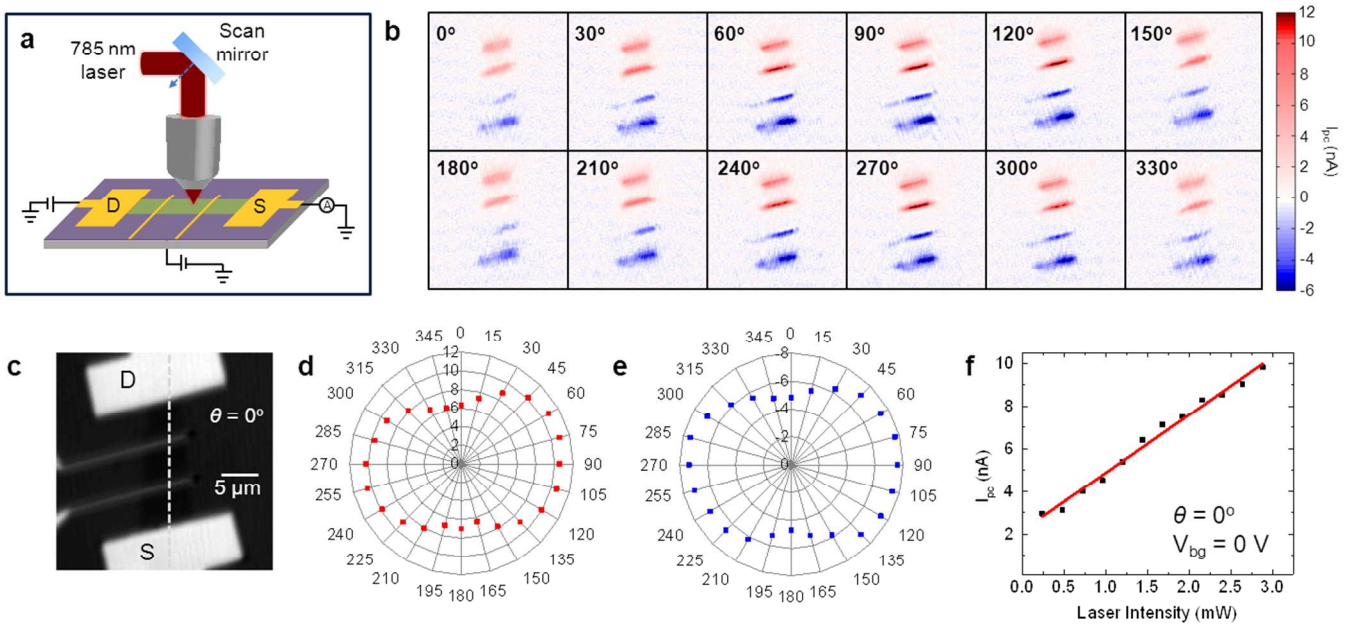

Figure 3. Polarization-photocurrent measurements of a BP FET at room temperature with a zero drain-source bias and V_{bg} = -10 V. (a) Schematic diagram of scanning photocurrent measurement setup. (b) Photocurrent image of the BP FET at different laser polarizations. (c) Corresponding grey-scale reflection image showing laser polarization direction at θ = 0°. The polarization dependence of strongest positive (red)/negative (blue) photocurrent response at the drain/source contact region is shown in (d) and (e), respectively. (f) Photocurrent intensities increase linearly with incident laser power measured at θ = 0°.

To explore the anisotropic nature of BP FETs, we performed spatially resolved polarization-dependent scanning photocurrent measurements on the BP FET (the inset of Fig 2b) in a Janis ST-500 Microscopy Cryostat under high vacuum (~ 1×10^{-6} Torr). As shown in Figure 3a, a diffraction-limited laser spot (λ = 785 nm, 1.58eV) was scanned over the BP FET by a two-axis scanning mirror with nanometer spatial resolution and photocurrent signals were recorded as a function of position, resulting in a spatially resolved photocurrent map of the device. The reflection of the incident laser beam was simultaneously recorded by a Si photodetector to locate the position of the sample. Figure 3b shows a series of photocurrent images recorded at different laser polarizations, where the polarization angle θ = 0° is indicated in the reflection image in Figure 3c. During the measurement, the two middle contacts were floating, and the photocurrent was measured between drain and source. In the reflection image, four gold electrodes are shown as light grey areas. The corresponding photocurrent images were recorded at a zero drain-source bias and V_{bg} = -10 V, where red/blue color corresponds to positive/negative current. The majority of photocurrent responses are observed in the four electrode regions where gold electrodes and the BP sample contact. At a zero drain-source bias, the strongest positive/negative photocurrent responses in the drain/source contact region for each map are shown in the polar plots in Figure 3d and 3e, respectively. The BP device shows a polarization-dependent photocurrent response, with the maximum signal intensity observed at θ around 75°/255° or along the x-axis, and the minimum intensity at θ around 165°/345° or along the y-axis. The photocurrent anisotropy ratio, $\sigma = (I_{pc}^{90^o} - I_{pc}^{0^o})/(I_{pc}^{90^o} + I_{pc}^{0^o})$ of the BP device is 0.3. The most likely reason for the anisotropy in the photocurrent response is the directional dependence of the interband transition strength in the anisotropic band structure of BP.[22] As demonstrated in previous experimental and theoretical studies, transitions between the highest valence and lowest conduction bands are allowed for the polarization along the x-axis ($\theta \approx$ 75°/255°), but partially forbidden for the polarization along the y-axis ($\theta \approx$ 165°/345°).[19, 21, 22] Therefore, more photons polarized along the x-axis than those along the y-axis can be absorbed and produce more electron-hole pairs, leading to stronger photocurrent responses. The magnitude of photocurrent against laser intensity is also explored, showing a linear relationship with incident laser intensity as illustrated in Figure 3f. The crystalline orientation of BP FET devices determined by polarization-dependent photocurrent is crucial to the understanding of the anisotropic transport properties of BP devices. These experimental results indicate that the relatively low mobility measured in Figure 2 can be partially attributed to the fact that the measured current flow was along the y direction (heavier effective mass).

To further investigate the photocurrent generation mechanisms in BP FETs, we performed gate-dependent scanning photocurrent measurements on BP transistors at 77 K, where the hysteresis behavior in the transfer characteristics is negligible as the charge trapping is suppressed at low temperatures.[16, 27, 28] Figure 4a and 4b display the reflection and photocurrent images of a BP FET at a zero drain-source bias with a gate voltage V_g = -30 V, respectively. By sweeping the gate voltage from -60 V to 60 V while recording the photocurrent along the channel direction of the BP FET (dashed line in Fig. 4a), we obtained the gate-dependent scanning photocurrent map (Fig. 4c). When the Fermi level moves from the valence band to the conduction band, the Schottky barrier height changes linearly with V_g: $\delta E_b = e\alpha V_g$, where E_b is the energy from the Fermi level to the nearest of the conduction and valence bands and α is a numerical constant that measures how effectively the gate modulates the band energies.[31-33] The measured shut-off gate voltages for *p-type* and *n-type* conductance are -12 V and 52 V, respectively (Fig. 4d, grey area). The electronic band is flattened at 14 V as indicated by the dashed line in Figure 4d. We also know that the band gap for few-layer BP crystals is 0.3 eV.[21] Therefore, the calculated $\alpha \approx 0.0047$ can be used to infer the Schottky barrier height to the conduction band: $\Phi_B = \Phi_m - \chi = 0.2\ V$.

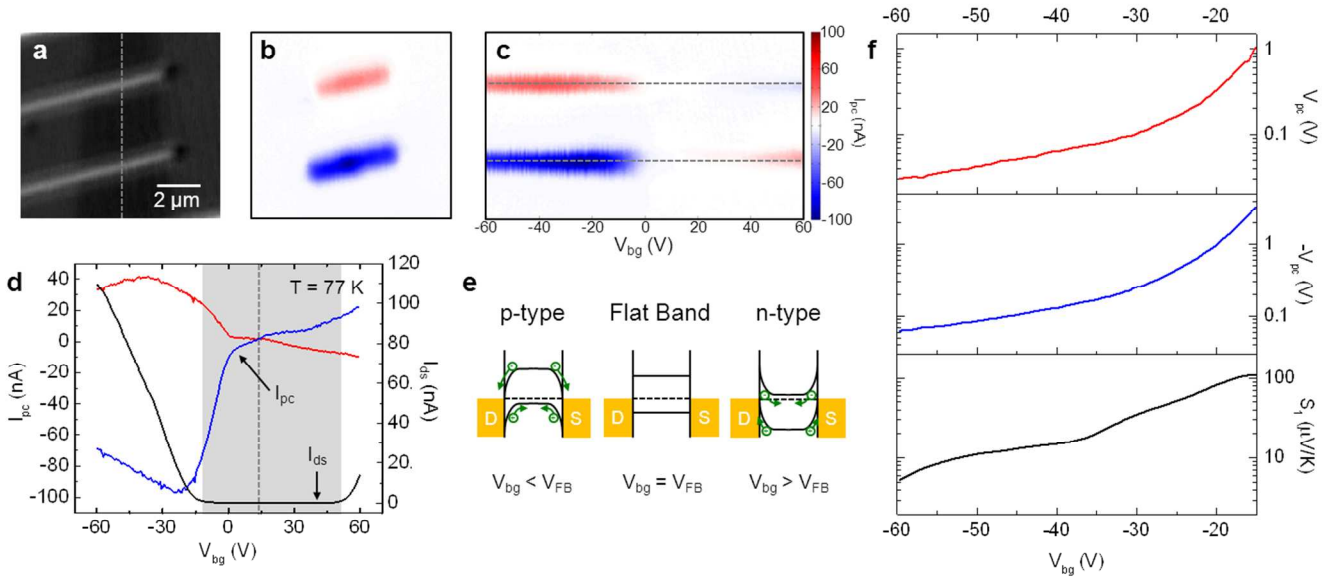

Figure 4. Gate-dependent photocurrent response of a BP FET at 77 K. (a) Reflection and (b) photocurrent images of a BP FET at V_{bg} = -30 V and a zero drain-source bias, respectively. (c) The gate-dependent scanning photocurrent images at a zero drain-source bias as V_{bg} varying from -60 V to 60 V. The laser scanning position is indicated by the white dotted line in (a). (d) The photocurrent responses along the horizontal cuts in (c) with a zero drain-source bias (red and blue curves, left) and drain current with a 100 mV drain-source bias (black curve, right) as a function of V_{bg}. The grey area illustrates the "off" state of the BP device and the dashed line indicates $V_{bg} = V_{FB}$. (e) Schematic diagrams of energy band diagrams illustrating the mechanisms of PVE. (f) The photovoltage signals ($V_{pc} = I_{pc}R$, red and blue curves) and the calculated Seebeck coefficient (black curve) at different V_{bg}.

As shown in Figure 4d, the photocurrent signal exhibits monotonic gate voltage dependence in the off-state (the grey area), indicating that the photovoltaic effect (PVE) plays an important role in its photocurrent generation. Upon laser excitation, electron-hole pairs will be generated locally and driven in opposite directions by the built-in electrical field owing to the Fermi level alignment that leads to Schottky barriers. In the p-type region (Fig. 4e *left*), since the electronic energies are lower near the contacts than in the middle of the BP device, electrons will be injected to the drain whereas holes will be annihilated by electrons from the source, resulting in a positive current flow. Likewise, electrons are injected into the source in the source electrode area and generate a negative current flow. The center of the device shows negligible photocurrent response due to the relatively flat band structure. When V_{bg} increases to 14 V, the rise of Fermi level flattens the band bending in the contact area, leading to a flat band structure (Fig. 4e *middle*). Similarly, an opposite polarity of photocurrent response is observed in the n-type region (Fig. 4e *right*).

Interestingly, the photocurrent signals show strong non-monotonic gate dependence when V_{bg} is lower than -15 V (Fig. 4d), which contradicts the prediction of the photovoltaic mechanisms. When light is absorbed by the BP, hot electron-hole pairs are generated. These electron-hole pairs can contribute directly to I_{pc} through PVE, but they can also locally heat the BP to produce photocurrent response via PTE. Because the Seebeck coefficient of BP (S_1) and the electrodes (S_2) are different, this local heating in the BP-electrode junction area will result in a voltage difference. The photovoltage due to PTE, V_{PTE}, can be expressed as

$$V_{PTE} = (S_1 - S_2)\Delta T$$

The Seebeck coefficient, S, can be derived from the Mott relation,[34-36]

$$S = -\frac{\pi^2 k_b^2 T}{3e}\frac{1}{G}\frac{dG}{dV_g}\frac{dV_g}{dE}\bigg|_{E=E_F}$$

where k_b is the Boltzmann constant, e is the electron charge, and E_F is the Fermi energy. The calculated Seebeck coefficient of BP S_1 is shown in Figure 4f (*bottom*). Notice that the Seebeck coefficient of metal electrodes S_2 has no gate dependence. As shown in Figure 4f *top* and *middle*, the photovoltage signals ($V_{pc} = I_{pc}R$, where I_{pc} is the photocurrent intensity and R is the resistance) have a similar gate dependence to the calculated thermoelectric power (S_1, Fig. 4f *bottom*).

Therefore, in addition to PVE, PTE is also likely to contribute to the photovoltage response generated at the BP-electrode junctions.

We also perform bias-dependent scanning photocurrent measurements on the BP FET at $V_{bg} = 0$ and different drain-source biases, from 0.2 V to – 0.2 V in a 0.1 V step (Fig. 5b). No significant photocurrent signal is observed in the middle of the BP crystal. The photocurrent responses on the electrode contact regions dominate even when a large bias is applied. A corresponding horizontal cut along the sample in each map is displayed in Figure 5a with an offset for clarity. At a positive bias, the intensity of the positive photocurrent response in the drain contact region is strongly enhanced. Similarly, the negative photocurrent intensity in the source contact region becomes much stronger when the device is negatively biased. Because the intensity of the photocurrent is roughly proportional to the local electrical field, or the slope of the electrostatic potential, we obtain qualitatively the electrostatic potential by integrating the photocurrent line cuts shown in Figure 5a. Figure 5c illustrates the resulting potential profile of the BP device. The potential change in different region at various biases can be easily identified. Large potential drops near the electrode contact regions and relatively flat band in the middle of the BP crystal are observed, indicating the presence of large contact resistances due to the Schottky barriers between electrodes and BP crystals and likely an addition tunneling barriers caused by the oxidation of BP in the contact regions. Further studies are needed to improve the electrical performance of BP FETs. Minimizing the exposure of the BP samples to the ambient conditions during the device fabrication process is expected to reduce the thickness of the oxidation layer between the electrode metal and BP sample. In addition, mild Argon plasma etching can be used to remove or reduce the oxidation layer right before the metal deposition. By selecting electrode metals with proper work functions, the Schottky barrier between electrode contacts and BP crystals may also be minimized.[30]

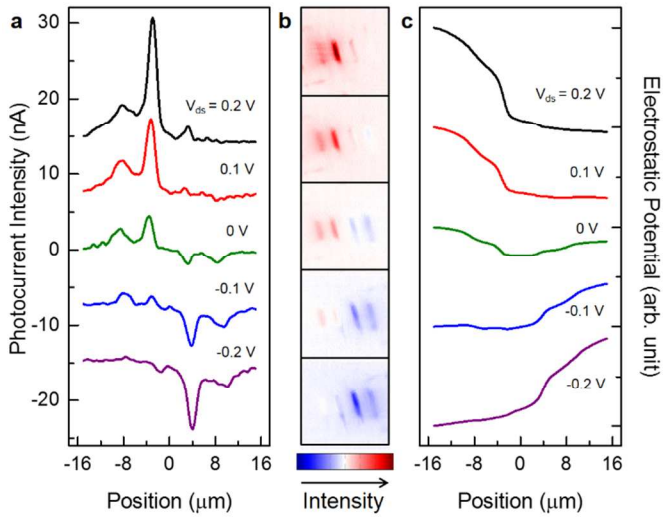

Figure 5. Bias dependence of a BP FET at V_{bg} = 0. The middle column (b) shows 30 μm x 30 μm scanning photocurrent images at different drain-source bias voltages from +0.2 V to -0.2 V with 0.1 V step. Red/blue color corresponds to the positive/negative photocurrent response, respectively. The left column (a) shows horizontal cross section cut in (b). The photocurrent intensity of each plot is offset by 8 nA. (c) Electrostatic potential deduced by integrating the photocurrent lines from the left column with an offset for clarity.

Conclusions

To conclude, STM measurements have been performed on freshly cleaved surfaces of BP crystals to characterize their qualities. We also report electrical transport and scanning photocurrent measurements of FETs made from few-layer BP crystals down to a few nanometers. In particular, we investigate the spatial-, polarization-, and gate-dependence of photocurrent in BP FETs. Our results reveal that the anisotropic feature of the photocurrent response near the BP-metal contact area primarily results from the directional-dependent absorption of BP crystals. The photocurrent signals generated at the junctions are mainly attributed to the built-in electric field (or PVE) in the off-state and thermoelectric power (or PTE) in the on-state. The estimated Seebeck coefficient of BP flakes (5-100 μV/K at 77 K) is comparable with graphene (1.5-15 μV/K at low temperature),[37-39] semiconducting carbon nanotubes (120-260 μV/K at 300 K),[40] and organic semiconductors (500-1000 μV/K at 208 K).[41] All these unique properties make few-layer BP crystal an ideal candidate for future 2D electronic, optoelectronic, and thermoelectric devices with unique anisotropic nature.

Acknowledgements

The BP FETs were fabricated at Wayne State University. Part of this research (STM measurements) was conducted at the Center for Nanophase Materials Sciences (CNMS), which is sponsored at Oak Ridge National Laboratory by the Office of Basic Energy Sciences, U.S. Department of Energy. This work was supported by the National Science Foundation (ECCS-1055852 and CBET-1264982 to YX; ECCS-1128297 and DMR-1308436 to ZZ).

Notes and references

[a] Department of Electrical Engineering and Computer Science, Vanderbilt University, Nashville, TN 37235.
[b] Department of Physics and Astronomy, Wayne State University, Detroit, MI 48201.
[c] Center of Nanophase Materials Sciences, Oak Ridge National Laboratory, TN, 37831.
[d] Department of Physics and Astronomy, Vanderbilt University, Nashville, TN 37235.

* To whom correspondence should be addressed, Email: yaqiong.xu@vanderbilt.edu, zxzhou@wayne.edu, and panm@ornl.gov.

1. P. Avouris, *Nano Letters*, 2010, **10**, 4285-4294.
2. P. Avouris, Z. H. Chen and V. Perebeinos, *Nature Nanotechnology*, 2007, **2**, 605-615.
3. K. S. Novoselov, A. K. Geim, S. V. Morozov, D. Jiang, Y. Zhang, S. V. Dubonos, I. V. Grigorieva and A. A. Firsov, *Science*, 2004, **306**, 666-669.
4. F. Bonaccorso, Z. Sun, T. Hasan and A. C. Ferrari, *Nat Photonics*, 2010, **4**, 611-622.
5. X. Du, I. Skachko, A. Barker and E. Y. Andrei, *Nature Nanotechnology*, 2008, **3**, 491-495.

6. Y. Q. Wu, Y. M. Lin, A. A. Bol, K. A. Jenkins, F. N. Xia, D. B. Farmer, Y. Zhu and P. Avouris, *Nature*, 2011, **472**, 74-78.
7. L. Liao, Y. C. Lin, M. Q. Bao, R. Cheng, J. W. Bai, Y. A. Liu, Y. Q. Qu, K. L. Wang, Y. Huang and X. F. Duan, *Nature*, 2010, **467**, 305-308.
8. B. Radisavljevic, A. Radenovic, J. Brivio, V. Giacometti and A. Kis, *Nature Nanotechnology*, 2011, **6**, 147-150.
9. H. Liu, A. T. Neal and P. D. D. Ye, *Acs Nano*, 2012, **6**, 8563-8569.
10. Y. Yoon, K. Ganapathi and S. Salahuddin, *Nano Letters*, 2011, **11**, 3768-3773.
11. H. Fang, S. Chuang, T. C. Chang, K. Takei, T. Takahashi and A. Javey, *Nano Letters*, 2012, **12**, 3788-3792.
12. H. Wang, L. L. Yu, Y. H. Lee, Y. M. Shi, A. Hsu, M. L. Chin, L. J. Li, M. Dubey, J. Kong and T. Palacios, *Nano Letters*, 2012, **12**, 4674-4680.
13. M. S. Fuhrer and J. Hone, *Nature Nanotechnology*, 2013, **8**, 146-147.
14. H. Liu, A. T. Neal, Z. Zhu, Z. Luo, X. Xu, D. Tománek and P. D. Ye, *Acs Nano*, 2014.
15. L. Li, Y. Yu, G. J. Ye, Q. Ge, X. Ou, H. Wu, D. Feng, X. H. Chen and Y. Zhang, *Nat Nano*, 2014, **advance online publication**.
16. S. P. Koenig, R. A. Doganov, H. Schmidt, A. H. Castro Neto and B. Özyilmaz, *Appl. Phys. Lett.*, 2014, **104**, 103106.
17. F. Xia, H. Wang and Y. Jia, *arXiv:1402.0270*, 2014.
18. M. Buscema, D. J. Groenendijk, S. I. Blanter, G. A. Steele, H. S. J. Van der Zant and A. Castellanos-Gomez, *arXiv:1403.0565*, 2014.
19. Y. Takao and A. Morita, *Physica B & C*, 1981, **105**, 93-98.
20. M. Baba, F. Izumida, A. Morita, Y. Koike and T. Fukase, *Jpn J Appl Phys 1*, 1991, **30**, 1753-1758.
21. Y. Akahama, S. Endo and S. Narita, *J Phys Soc Jpn*, 1983, **52**, 2148-2155.
22. A. Morita, *Appl Phys a-Mater*, 1986, **39**, 227-242.
23. C. D. Zhang, J. C. Lian, W. Yi, Y. H. Jiang, L. W. Liu, H. Hu, W. D. Xiao, S. X. Du, L. L. Sun and H. J. Gao, *J Phys Chem C*, 2009, **113**, 18823-18826.
24. K. S. Novoselov, D. Jiang, F. Schedin, T. J. Booth, V. V. Khotkevich, S. V. Morozov and A. K. Geim, *Proceedings of the National Academy of Sciences of the United States of America*, 2005, **102**, 10451-10453.
25. M. M. Perera, M.-W. Lin, H.-J. Chuang, B. P. Chamlagain, C. Wang, X. Tan, M. M.-C. Cheng, D. Tománek and Z. Zhou, *Acs Nano*, 2013, **7**, 4449-4458.
26. M.-W. Lin, C. Ling, L. A. Agapito, N. Kioussis, Y. Zhang, M. M.-C. Cheng, W. L. Wang, E. Kaxiras and Z. Zhou, *Phys. Rev. B*, 2011, **84**, 125411.
27. D. J. Late, B. Liu, R. H. S. S. Matte, V. P. Dravid and C. N. R. Rao, *Acs Nano*, 2012, **6**, 5635–5641.
28. H. Wang, Y. Wu, C. Cong, J. Shang and T. Yu, *Acs Nano*, 2010, **4**, 7221-7228.
29. W. Liu, J. Kang, D. Sarkar, Y. Khatami, D. Jena and K. Banerjee, *Nano Lett.*, 2013, **13**, 1983-1990.
30. S. Das, H.-Y. Chen, A. V. Penumatcha and J. Appenzeller, *Nano Lett.*, 2012, **13**, 100-105.
31. S. Rosenblatt, Y. Yaish, J. Park, J. Gore, V. Sazonova and P. L. McEuen, *Nano Letters*, 2002, **2**, 869-872.
32. Y. Ahn, J. Dunning and J. Park, *Nano Letters*, 2005, **5**, 1367-1370.
33. M. Freitag, J. C. Tsang, A. Bol, D. N. Yuan, J. Liu and P. Avouris, *Nano Letters*, 2007, **7**, 2037-2042.
34. M. Cutler and N. F. Mott, *Phys Rev*, 1969, **181**, 1336-&.
35. M. Buscema, M. Barkelid, V. Zwiller, H. S. J. van der Zant, G. A. Steele and A. Castellanos-Gomez, *Nano Letters*, 2013, **13**, 358-363.
36. Y. M. Zuev, W. Chang and P. Kim, *Physical Review Letters*, 2009, **102**.
37. J. H. Seol, I. Jo, A. L. Moore, L. Lindsay, Z. H. Aitken, M. T. Pettes, X. S. Li, Z. Yao, R. Huang, D. Broido, N. Mingo, R. S. Ruoff and L. Shi, *Science*, 2010, **328**, 213-216.
38. X. D. Xu, N. M. Gabor, J. S. Alden, A. M. van der Zande and P. L. McEuen, *Nano Letters*, 2010, **10**, 562-566.
39. N. M. Gabor, J. C. W. Song, Q. Ma, N. L. Nair, T. Taychatanapat, K. Watanabe, T. Taniguchi, L. S. Levitov and P. Jarillo-Herrero, *Science*, 2011, **334**, 648-652.
40. J. P. Small, K. M. Perez and P. Kim, *Physical Review Letters*, 2003, **91**.
41. K. P. Pernstich, B. Rossner and B. Batlogg, *Nat Mater*, 2008, **7**, 321-325.

